PAPER

Synthesis of Y_2O_3:Bi^{3+},Eu^{3+} nanosheets from layered yttrium hydroxide precursor and their photoluminescence properties†

Tomotaka Watanabe, Yoshiki Iso* and Tetsuhiko Isobe*

We produced Y_2O_3:Bi^{3+},Eu^{3+} nanosheets by calcining layered yttrium hydroxide (LYH) precursor nanosheets at 800 °C for 2 h. The precursor nanosheets were synthesized from metallic chlorides dissolved in methanol, *via* a solvothermal reaction at 200 °C for 2.5 h. X-ray diffraction and transmission electron microscopy revealed that the LYH nanosheets were composed of crystallites with a uniform crystallographic orientation. Their sheet-like morphology and single-crystal nature remained after calcination, while the thickness of the nanosheets decreased. Their excitation spectrum was monitored at the 612 nm emission wavelength, corresponding to the $^5D_0 \rightarrow {}^7F_2$ transition of Eu^{3+}, and featured a broad band at 332 nm that was attributed to the $6s^2 \rightarrow 6s6p$ transition of Bi^{3+}. The Y_2O_3:Bi^{3+},Eu^{3+} nanosheets therefore exhibited red emission from Eu^{3+} *via* energy transfer from Bi^{3+} to Eu^{3+} following near-UV excitation of Bi^{3+}. The photoluminescence (PL) properties of the calcined samples were investigated with various concentrations of Bi^{3+} in Y_2O_3 nanosheets codoped with 2 at% Eu^{3+}. The highest PL quantum yield was 23% at a Bi^{3+} concentration of 0.2 at%. The PL lifetimes of the calcined samples decreased with increasing Bi^{3+} concentration due to concentration quenching. The PL intensity increased over time under continuous excitation, which might be attributable to the photooxidation of Bi following its reduction by polyethyleneimine or methanol during the LYH synthesis.

1 Introduction

Y_2O_3 doped with Eu^{3+} (Y_2O_3:Eu^{3+}) shows strong red emission under ultraviolet (UV) light *via* the charge–transfer transition of $O^{2-} \rightarrow Eu^{3+}$.[1-3] It is well known that the codopant Bi^{3+} acts as a sensitizer for Eu^{3+} *via* energy transfer from Bi^{3+} to Eu^{3+} following the $6s^2 \rightarrow 6s6p$ transition of Bi^{3+} under near-UV excitation.[4-6] Y_2O_3 codoped with Bi^{3+} and Eu^{3+} (Y_2O_3:Bi^{3+},Eu^{3+}) therefore shows red emission from Eu^{3+} excited by near-UV excitation at wavelengths of around 300–400 nm. Y_2O_3:Bi^{3+},Eu^{3+} has attracted attentions for an application to wavelength-conversion material in white light-emitting diodes,[7] while Y_2O_3:Eu^{3+} had been used in the traditional cathode ray tube.[8]

Department of Applied Chemistry, Faculty of Science and Technology, Keio University, 3-14-1 Hiyoshi, Kohoku-ku, Yokohama 223-8522, Japan. E-mail: iso@applc.keio.ac.jp; isobe@applc.keio.ac.jp; Fax: + 81 45 566 1551; Tel: +81 45 566 1558; +81 45 566 1554

† Electronic supplementary information (ESI) available: TG-DTA thermograms of undoped, 10 at% Bi^{3+}-doped, and 2 at% Eu^{3+}-doped precursors (Fig. S1); high-precision (220) XRD peaks and (222) XRD peaks of undoped, 10 at% Bi^{3+}-doped, 2 at% Eu^{3+}-doped, and Bi^{3+},Eu^{3+}-codoped LYH precursors and Y_2O_3 samples, respectively (Fig. S2); calculated d-spacings and crystallite sizes from Fig. S2 (Tables S1 and S2); AFM images of an LYH precursor nanosheet and a Y_2O_3 nanosheet, codoped with 10 at% Bi^{3+} and 2 at% Eu^{3+} (Fig. S3); XRD profiles, atomic compositions determined by XRF, and PL and PLE spectra of x at% Bi^{3+},2 at% Eu^{3+}-codoped Y_2O_3 samples (Fig. S4, Table S3, and Fig. S5, respectively). See DOI: 10.1039/c7ra01114h

In recent years, one of the potential applications of phosphors such as these, which absorb near-UV light, is as a spectral converter to improve the photoelectric conversion efficiency of solar cells.[9-13] The sensitivity of commercial silicon solar modules is low in the UV region because of reflection and absorption by encapsulation materials.[13] Thermalization losses following the absorption of photons with excess energy also reduce the sensitivity.[14] A spectral converter converts near-UV light to visible light, from which the solar modules can generate electricity more efficiently. The fluorescent film used for spectral converters requires transparency in the visible range to prevent the loss of visible sunlight. In addition, the phosphors for spectral converters must have high stability under sunlight, *i.e.*, light-fastness and thermal stability. Inorganic nanophosphors, such as YVO_4:Bi^{3+},Eu^{3+} nanoparticles, can satisfy those requirements. YVO_4:Bi^{3+},Eu^{3+} nanoparticles, which show red emission under near-UV excitation, exhibit high transparency because of their low light-scattering loss. Previously, we reported transparent films fabricated by dispersing YVO_4:Bi^{3+},Eu^{3+} nanoparticles in a polyurethane matrix.[15] The fabricated films could convert near-UV light to red light and had high transparency in the visible range. However, exposure to near-UV irradiation also decreased the photoluminescence (PL) intensity of the films. Under near-UV excitation, YVO_4:Bi^{3+},Eu^{3+} reacted photochemically with the polyurethane matrix and with

citrate ions adsorbed on the surfaces of the nanoparticles, which resulted in the reduction of V^{5+} to V^{4+}.[16–18]

In contrast to YVO_4:Bi^{3+},Eu^{3+} nanoparticles, Y_2O_3:Bi^{3+},Eu^{3+} is composed of chemically stable ions. In addition, Y_2O_3 is not semiconductive, which means it does not behave as a photo-catalyst under near-UV irradiation. It is reported that Y_2O_3:Eu^{3+} nanosheets can be obtained *via* the calcination of yttrium hydroxides, and that they are suitable for transparent phosphor films.[19] For those reasons, Y_2O_3:Bi^{3+},Eu^{3+} nanosheets represent a promising material for spectral converters.

Y_2O_3:Eu^{3+} nanophosphors have mostly been produced *via* the calcination of precursors.[1,2,20–22] Recently, Y_2O_3:Eu^{3+} nanosheets prepared from layered rare earth hydroxide (LRH; $RE_2(OH)_5$-A·nH_2O; RE = Y, Eu, A = free anions) were reported.[23] LRHs contain host layers composed of planar rare earth hydroxides, with H_2O molecules and free anions intercalated in the inter-layers.[24] The host layer is a close-packed crystal plane, so LRHs tend to become nanosheets through crystallization along the (001) plane.[25] Furthermore, [111]-oriented oxide nanosheets can be obtained from the corresponding [001]-oriented LRH nanosheets *via* quasi-topotactic transformation under calcinations.[26] Highly [111]-oriented and transparent rare earth oxide films can be fabricated by the deposition of LRH nanosheets onto a substrate followed by calcinations.[24,27,28] LRH nanosheets have drawn attention as precursors for highly oriented and transparent films.

Very recently, we fabricated Y_2O_3:Bi^{3+},Eu^{3+} nanosheets using nitrates as the starting reagents, and these nanosheets showed high photostability under near-UV excitation.[29] In the synthesis, ethylene glycol was used as a solvent for bismuth nitrate ($Bi(NO_3)_3$·$5H_2O$) because bismuth nitrate is not soluble in water. The concentration of Bi^{3+} in the Y_2O_3:Bi^{3+},Eu^{3+} nanosheets was lower than the nominal value, probably because of the high stability of bismuth ions coordinated with ethylene glycol. In the present work, we chose bismuth chloride ($BiCl_3$) as an alternative bismuth source. Although bismuth chloride is only sparingly soluble in alcohols under ambient conditions, its solubility is increased under the high-temperature conditions of solvothermal synthesis. In the present work, we synthesized nanosheets of layered yttrium hydroxide codoped with Bi^{3+} and Eu^{3+} (LYH:Bi^{3+},Eu^{3+}) in a mixture of chlorides in methanol and a poly-ethyleneimine (PEI) aqueous solution, inside an autoclave. We then synthesized Y_2O_3:Bi^{3+},Eu^{3+} nanosheets *via* the calcination of these LYH precursors, and measured their photoluminescent properties.

2 Experimental section

2.1 Materials

YCl_3·$6H_2O$ (99.99%), $BiCl_3$ (99.5%), and methanol (99.8%) were purchased from Kanto Chemical. $EuCl_3$·$6H_2O$ (99.9%) was purchased from Soekawa Chemical. PEI (M_w = 25 000, 99%) was purchased from Sigma-Aldrich. All reagents were used without further purification.

2.2 Preparation of precursors and calcined sample

YCl_3·$6H_2O$, $EuCl_3$·$6H_2O$, and $BiCl_3$ (total 0.5 mmol, Eu = 2 at%, Bi = 0.1–10 at%) were added to 16 mL of methanol. Then,

the mixture was added into 5 mL of 2 wt% PEI aqueous solu-tion. The resulting suspension was placed in a Teflon vessel with a volume of 50 mL and heated in a stainless steel auto-clave (Berghof, DAB-2) at 200 °C for 2.5 h. After cooling to room temperature, the precipitate was isolated by washing with ethanol, followed by 5 min of centrifugation at 11 000 × g (10 000 rpm using a rotor with a diameter of 10 cm). This cycle of washing and centrifugation was performed twice. The precipitate was then dried at 60 °C for 5 h to obtain a precursor codoped with Bi^{3+} and Eu^{3+}. An undoped precursor, as well as precursors singly doped with either Bi^{3+} or Eu^{3+}, were also prepared by the same procedure. The precursors were heated to 800 °C at a heating rate of 10 °C min^{-1} in an air flow of 300 mL min^{-1}, and kept at that temperature for 2 h to obtain the calcined samples.

2.3 Characterization

Thermal analysis was performed using a thermogravimetry and differential thermal analysis (TG-DTA) instrument (Thermo Plus-8120, Rigaku) at a heating rate of 10 °C min^{-1} in an air flow of 300 mL min^{-1}. X-ray diffraction (XRD) patterns were measured on an X-ray diffractometer (Rint-2200, Rigaku) with a Cu Kα radiation source and monochromator. Elemental compositions were determined by the funda-mental parameter method using an X-ray fluorescence (XRF) analyzer (ZFX mini II, Rigaku). Particles were observed with a transmission electron microscope (TEM; Tecnai G^2 and Tecnai 12, FEI). The samples for TEM were prepared by drying a drop of a methanol dispersion of each sample on a carbon-reinforced collodion film of a copper grid. The topographies of the nanosheets were observed with an atomic force microscope (AFM; AFM5100N, Hitachi) in dynamic mode using a cantilever (Pointprobe NCHR, Nano world). The samples for AFM were prepared by drying a drop of a meth-anol dispersion of each sample on a negative-type silicon wafer. PL and photoluminescence excitation (PLE) spectra were recorded on a fluorescence spectrometer (FP-6500, JASCO). Changes in PL intensity during continuous near-UV excitation were measured with the same apparatus. Each spectral response was calibrated using an ethylene glycol solution of Rhodamine B (5.5 g L^{-1}) and a standard light source (ESC-333, JASCO). The PL quantum yield (QY), Φ, was measured on the same spectrometer equipped with an inte-grating sphere (ISF-513, JASCO), based on the following equation:

$$\Phi = \frac{I_{em}}{I_{ex} - I_{ref}} \qquad (1)$$

where I_{em} is the integrated emission intensity of the sample, I_{ex} is the integrated intensity of the incident excitation light, and I_{ref} is the integrated intensity of the excitation light reflected by the sample. A reflectance standard (Spectralon SRS-99, Lab-sphere) was used to determine I_{ex}. PL decay curves were recor-ded on a fluorescent lifetime spectrometer (Quantaurus-Tau C11367, Hamamatsu Photonics) using a Xe flash lamp with a band path filter of 365 nm.

3 Results and discussion

3.1 Particulate and structural properties of precursors and of samples calcined at 800 °C

The TG-DTA profiles (Fig. 1) of the precursor codoped with 10 at% Bi^{3+} and 2 at% Eu^{3+} show the endothermic weight loss proceeding in three steps, which are similar to those previously observed for $Ln_2(OH)_5NO_3 \cdot nH_2O$.[23,30] In the case of $Y_2(OH)_5$-$Cl \cdot nH_2O$ herein, the first step, occurring below 145 °C, corresponds to the evaporation of co-intercalated water. The second step, at 300 °C, corresponds to the dehydration of the host layers. The third step, at 800 °C, corresponds to the evaporation of intercalated anions. The third step occurred at a higher temperature than for $Ln_2(OH)_5NO_3 \cdot nH_2O$, possibly because of the higher charge density of chloride ions. All the precursors showed qualitatively similar TG-DTA thermograms (Fig. S1†).

The XRD patterns (Fig. 2) of all the precursors were indexed to orthorhombic $Y_2(OH)_5Cl \cdot nH_2O$, as reported by Liang et al.[31] The high-precision XRD profiles (Fig. S2(A) and Table S1†) indicated a shift of the (220) reflection to the lower-angle side in the doped samples. This indicates an expansion of the metal-to-metal distances in the LYH host layers[23] caused by the substitution of Bi^{3+} and Eu^{3+} (with their larger ionic radii) for Y^{3+}. The crystallite sizes of the precursors, calculated from the widths of the (220) reflection peaks using the Scherrer equation, were approximately 60–70 nm. The TEM images revealed that all the precursors obtained after autoclaving possessed an elongated sheet-like shape, as shown in panels (a)–(d) of Fig. 3. The lateral sizes of the nanosheets were on the order of hundreds of nanometers. The crystallite sizes determined from the (220) reflection peaks were thus smaller than the lateral sizes, indicating that the precursors were polycrystalline. The thickness of the nanosheets measured by AFM (Fig. S3(A)†) was 40 nm, which corresponds to ∼50 layers. Panel (b) of Fig. 4 shows a selected-area electron diffraction (SAED) image of one Bi^{3+},Eu^{3+}-codoped precursor nanosheet (panel (a) of Fig. 4), which exhibits a spot pattern of LYH.[32] This indicates that each nanosheet was composed of crystallites with a uniform crystallographic orientation; i.e., they had a single-crystal nature.
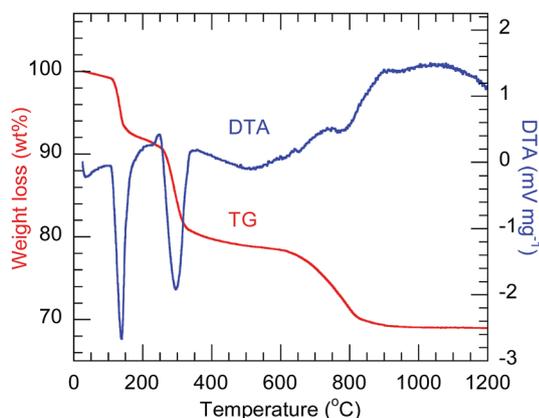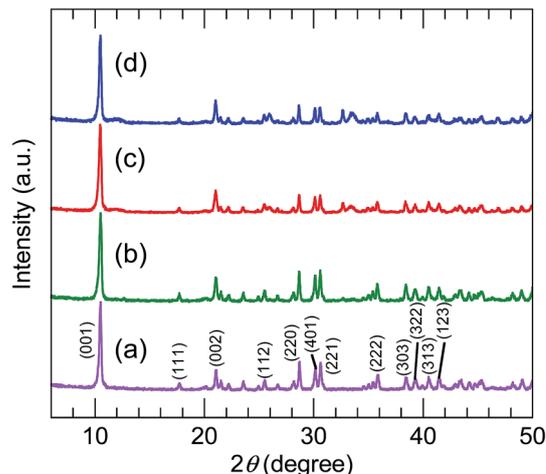

Fig. 2 XRD profiles of (a) undoped, (b) 10 at% Bi^{3+}-doped, (c) 2 at% Eu^{3+}-doped, and (d) 10 at% Bi^{3+},2 at% Eu^{3+}-codoped precursors.

The high-resolution TEM image of the selected nanosheet (panel (c) of Fig. 4) showed lattice fringes representing the (220) plane, with a spacing of 0.31 nm. The fast Fourier transform (FFT) image in panel (d) of Fig. 4 is similar to the SAED pattern.

Table 1 shows the metallic compositions of the precursors as measured by XRF. The measured Eu contents of the Bi^{3+},Eu^{3+}-codoped and Eu^{3+}-doped precursors were larger than their nominal contents, while the measured Y contents of both precursors were smaller than their nominal contents. The measured Bi content of the Bi^{3+},Eu^{3+}-codoped precursor, 8.4 at%, was smaller than the nominal content (10 at%), while that of the Bi^{3+}-doped precursor, 14.3 at%, was larger than the nominal content (10 at%). In our previous research, in which metallic nitrates were used as starting materials, the Bi^{3+}-doped and Bi^{3+},Eu^{3+}-codoped precursors with nominal Bi contents of 10 at% had measured Bi contents of 2.8 and 3.4 at%, respectively,[29] both smaller than those in this work. In that study, bismuth nitrate was dissolved in ethylene glycol, to allow Bi^{3+} to form a stable complex in solution and prevent Bi^{3+} ions from precipitating. In summary, the XRF results show that precursors with the desired Bi contents can be easily synthesized by our proposed method, in which metallic chlorides are used as starting materials. This method therefore enables research into the effect of the Bi content on the morphological characteristics and PL properties of nanosheets.

The XRD patterns of the samples calcined at 800 °C (Fig. 5) were consistent with pure-phase cubic Y_2O_3. The high-precision XRD profiles (Fig. S2(B) and Table S2†) indicated a shift of the (222) reflection to the lower-angle side in the doped samples. This indicates an expansion of the d-spacing of the (222) facets caused by the substitution of Bi^{3+} and Eu^{3+} (with their larger ionic radii) for Y^{3+}. The crystallite size of the nanosheets, calculated from the width of the (222) reflection peak using the Scherrer equation, was 19–20 nm. The TEM images of the samples calcined at 800 °C (panels (e)–(h) of Fig. 3) revealed that the elongated nanosheets remained unchanged after calcination, while the thickness of the nanosheets obtained by AFM (Fig. S3†) decreased from 40 nm to 25 nm. Panel (b) of Fig. 6 shows an
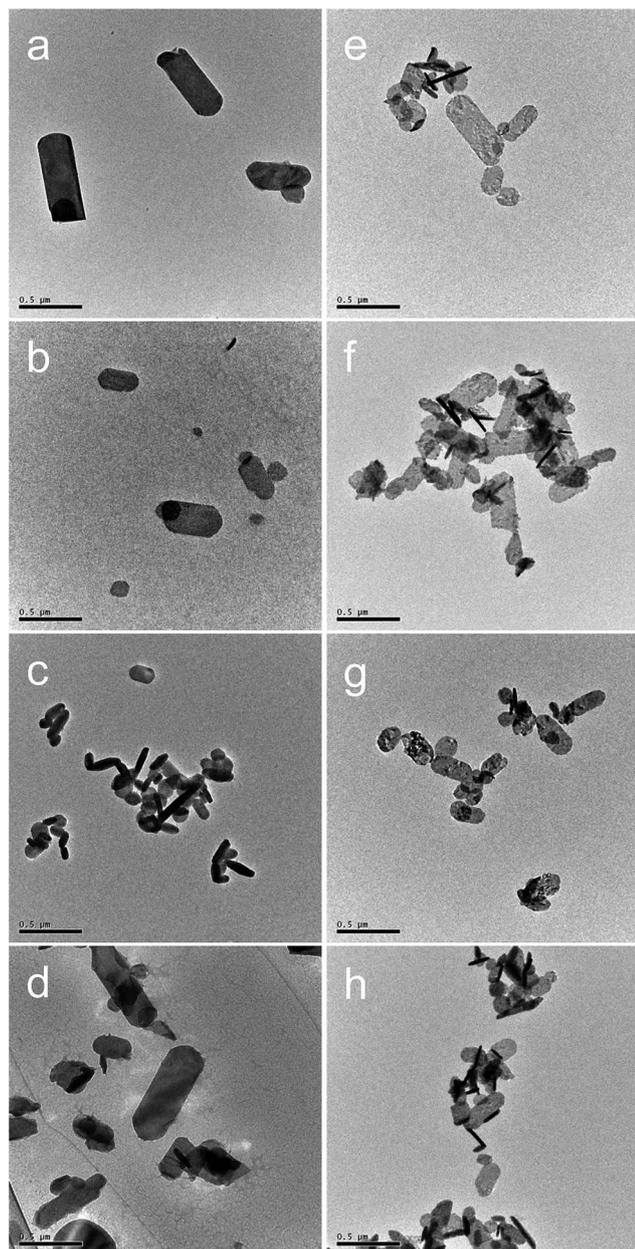

Fig. 1 TG-DTA thermograms of the 10 at% Bi^{3+},2 at% Eu^{3+}-codoped precursor.

Fig. 3 TEM images of (a–d) precursors and (e–h) samples calcined at 800 °C for 2 h with different dopants: (a, e) undoped, (b, f) 10 at% Bi^{3+}-doped, (c, g) 2 at% Eu^{3+}-doped, and (d, h) 10 at% Bi^{3+},2 at% Eu^{3+}-codoped. Scale bar: 0.5 μm.

Fig. 4 (a) TEM image, (b) SAED pattern, (c) high-resolution TEM image, and (d) FFT image of a 10 at% Bi^{3+},2 at% Eu^{3+}-codoped precursor nanosheet.

Table 1 Atomic compositions of precursors and calcined samples determined by XRF

Dopant(s)	Sample	Y (at%)	Bi (at%)	Eu (at%)
Eu^{3+}	Nominal	98.0	0.0	2.0
	Precursor	91.3	0.0	8.7
	Calcined	94.4	0.0	5.6
Bi^{3+}	Nominal	90.0	10.0	0.0
	Precursor	85.7	14.3	0.0
	Calcined	88.7	11.3	0.0
Bi^{3+},Eu^{3+}	Nominal	88.0	10.0	2.0
	Precursor	85.8	8.4	5.8
	Calcined	86.2	9.0	4.8

SAED image of one Y_2O_3:Bi^{3+},Eu^{3+} nanosheet (panel (a) of Fig. 6), which also exhibits a spot pattern. This indicates that the nanosheets retained their single-crystal nature. The high-resolution TEM image of the selected nanosheet (panel (c) of Fig. 6) showed lattice fringes representing the (211) plane of cubic Y_2O_3, with a spacing of 0.43 nm. The FFT image in panel (d) of Fig. 6 also exhibits a spot pattern corresponding to cubic Y_2O_3.

3.2 PL properties of samples calcined at 800 °C

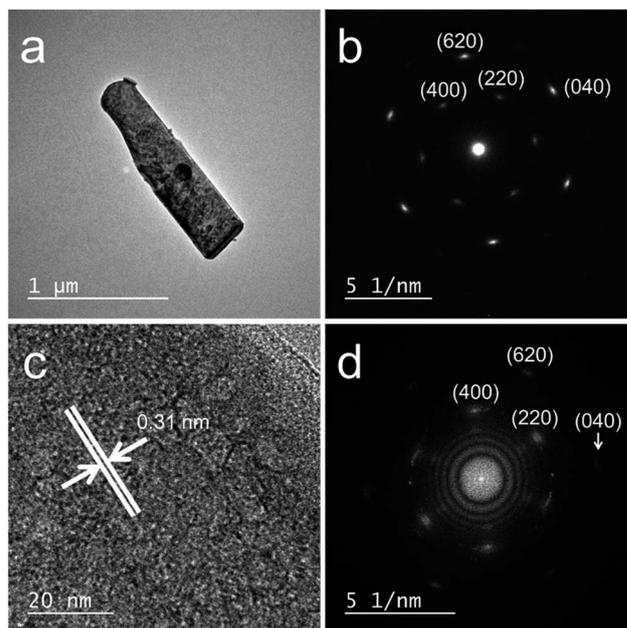Fig. 7 shows the PL and PLE spectra of the samples calcined at 800 °C. The Y_2O_3:Bi^{3+} nanosheets showed broad emission at 502 nm under excitation at 332 nm, arising from the transition between the $6s^2$ and $6s6p$ orbitals of Bi^{3+}.[2] For the Y_2O_3:Eu^{3+} nanosheets, sharp emission peaks corresponding to the $^5D_0 \rightarrow {^7F_J}$ ($J = 1$–4) transitions of Eu^{3+} were observed at 593, 612, 652, and 710 nm, respectively, under excitation at 234 nm, arising from $O^{2-} \rightarrow Eu^{3+}$ charge transfer.[3] For the Y_2O_3:Bi^{3+},Eu^{3+} nanosheets, a strong $^5D_0 \rightarrow {^7F_2}$ emission from Eu^{3+} was observed at 612 nm under 332 nm excitation. This arose from the energy transfer from excited Bi^{3+} to Eu^{3+}.[4] Y_2O_3 contains two distinct cation sites with different symmetries (S_6 and C_2). The $^5D_0 \rightarrow {^7F_2}$ transition of Eu^{3+} is forbidden under inversion symmetry, so the $^5D_0 \rightarrow {^7F_2}$ emission of the Y_2O_3:Bi^{3+},Eu^{3+} nanosheets must be predominantly attributed to Eu^{3+} ions at the C_2 sites and at sites on the surface without inversion symmetry.

The PL QY of the calcined sample codoped with 10 at% Bi^{3+} and 2 at% Eu^{3+} was less than 1%. It is known that concentration quenching occurs when the Bi content exceeds a certain level.
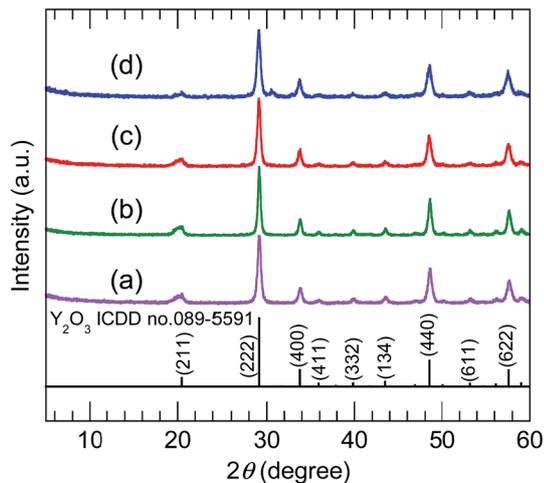
Fig. 5 XRD profiles of (a) undoped, (b) 10 at% Bi^{3+}-doped, (c) 2 at% Eu^{3+}-doped, and (d) 10 at% Bi^{3+},2 at% Eu^{3+}-codoped calcined samples.
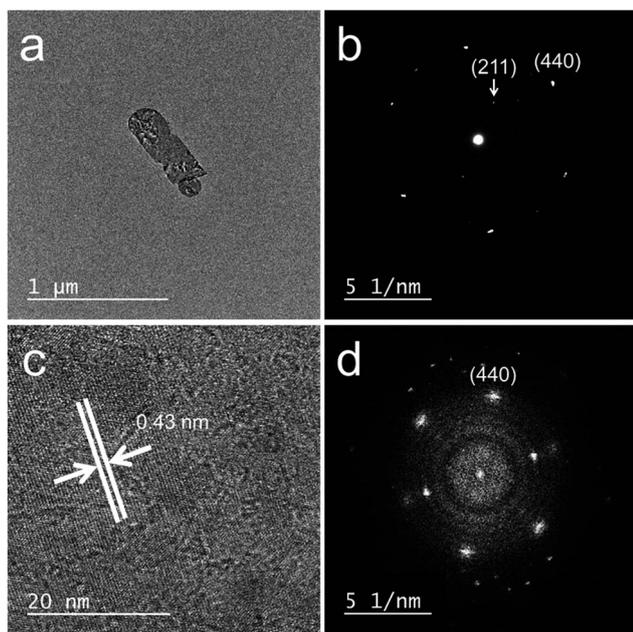

Fig. 6 (a) TEM image, (b) SAED pattern, (c) high-resolution TEM image, and (d) FFT image of a 10 at% Bi^{3+},2 at% Eu^{3+}-codoped calcined nanosheet.

Fig. 7 PL and PLE spectra of (a) x at% Bi^{3+}-doped, (b) 2 at% Eu^{3+}-doped and (c) x at% Bi^{3+},2 at% Eu^{3+}-codoped calcined samples. (a) $\lambda_{ex} = 332$ nm and $\lambda_{em} = 502$ nm, (b) $\lambda_{ex} = 210$ nm and $\lambda_{em} = 612$ nm, (c) $\lambda_{ex} = 332$ nm and $\lambda_{em} = 612$ nm.

Therefore, a series of samples with lower concentrations of Bi (0.1–10 at%), each codoped with Eu at a fixed concentration of 2 at%, was synthesized. All of these samples had the same crystal structure, belonging to cubic Y_2O_3, and their Bi and Eu concentrations were found to be close to the nominal values (Fig. S4 and Table S3†). The samples with different Bi concentrations exhibited PL and PLE peaks with the same shapes but different intensities (Fig. S5†). Fig. 8 shows the variation in the PL QY of the calcined Bi^{3+},Eu^{3+}-codoped samples as a function of the nominal Bi concentration.

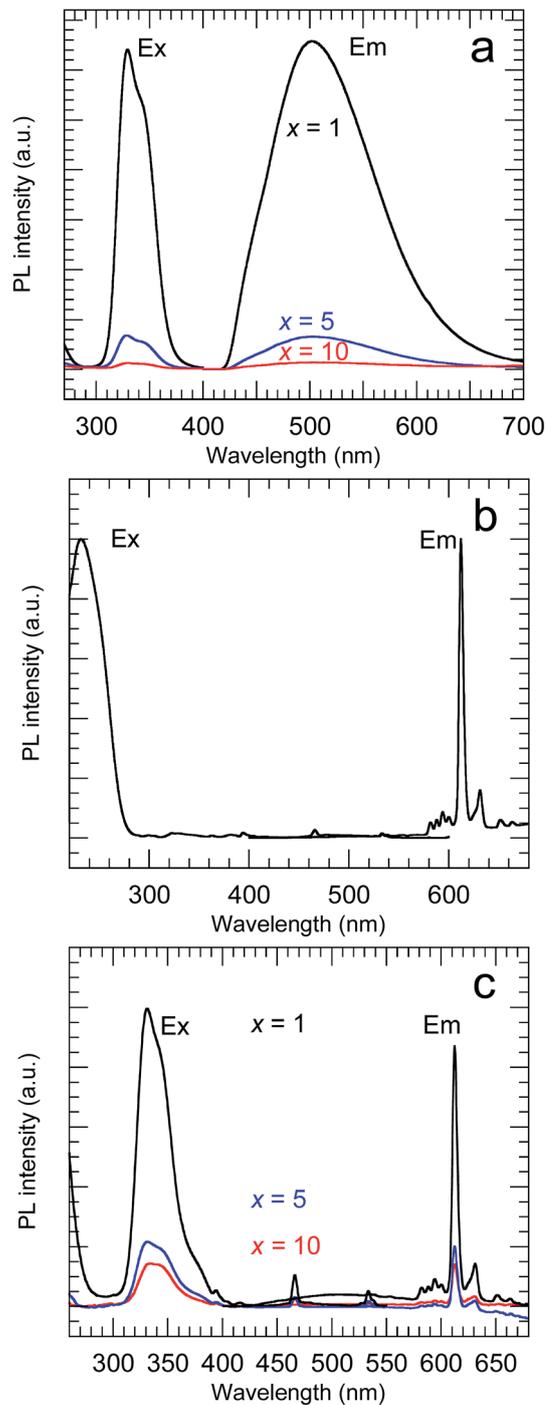The highest PL QY was 23%, for the sample with a Bi concentration of 0.2 at%. The decay characteristics of the calcined samples also showed a dependence on the Bi^{3+} concentration, as shown in Fig. 9 and Table 2. The PL decay curves for the 612 nm emission from Eu^{3+} can be well fitted by eqn (2):

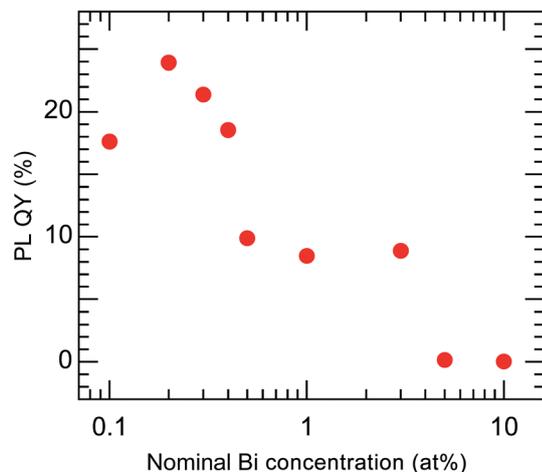$$I = A_1 \exp(-t/\tau_1) + A_2 \exp(-t/\tau_2) \qquad (2)$$

Fig. 8 PL QY of Bi^{3+},Eu^{3+}-codoped calcined samples with varying nominal Bi concentrations. Eu^{3+} = 2 at%. λ_{ex} = 332 nm and λ_{em} = 612 nm.
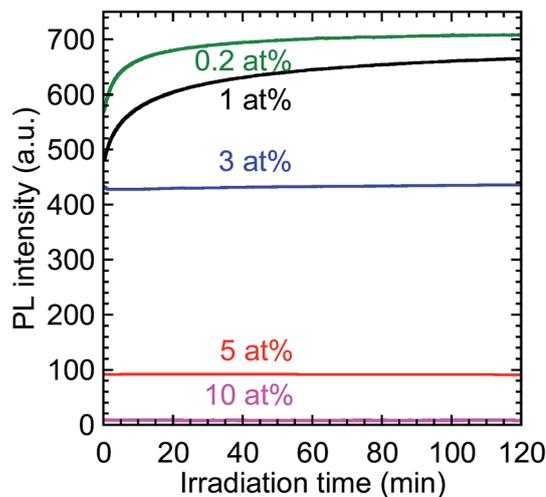

Fig. 10 Time-evolution of the PL intensity of the calcined samples codoped with 0.2–10 at% Bi^{3+} and 2 at% Eu^{3+} under continuous near-UV excitation. λ_{ex} = 332 nm and λ_{em} = 612 nm.

$$\tau = (A_1\tau_1^2 + A_2\tau_2^2)(A_1\tau_1 + A_2\tau_2) \tag{3}$$

τ was found to decrease with increasing Bi^{3+} concentration, which confirmed that concentration quenching occurred with $\geq$0.2 at% Bi^{3+}.

The time-evolution of the PL intensity of the 612 nm emission from the Y_2O_3:Bi^{3+},Eu^{3+} nanosheets under continuous excitation was measured to evaluate their photostability; the results are presented in Fig. 10. The initial PL intensity was highest for the calcined sample codoped with 0.2 at% Bi^{3+} and 2 at% Eu^{3+}. For the samples with the low Bi contents, the PL intensity prominently increased soon after the excitation began. For example, with 0.2 at% Bi^{3+}, the PL intensity increased to 120% of its initial value, and then remained constant. Such an increase in PL intensity under continuous excitation has, to the best of our knowledge, never been reported for Y_2O_3:Bi^{3+},Eu^{3+}. This behavior may be attributable to the photooxidation of bismuth ions in the calcined samples. Bismuth has a variety of possible valence states, including Bi^+ and Bi^{2+}.[33] If the Bi^{3+} ions were reduced to those species by PEI or methanol during the synthesis, the subsequent photooxidation of Bi^+ or Bi^{2+} back to Bi^{3+} would increase the number of excitation centers. This may be the origin of the increased PL intensity of the samples with low Bi concentrations, such as 0.2 at%. In the samples with higher Bi concentrations, the increase in PL intensity following excitation was markedly smaller. Increasing the Bi^{3+} concentration would have shortened the distances between Bi^{3+} ions and increased the probability of energy transfer between them, a process that contributes to concentration quenching, thus suppressing the increase in PL intensity.

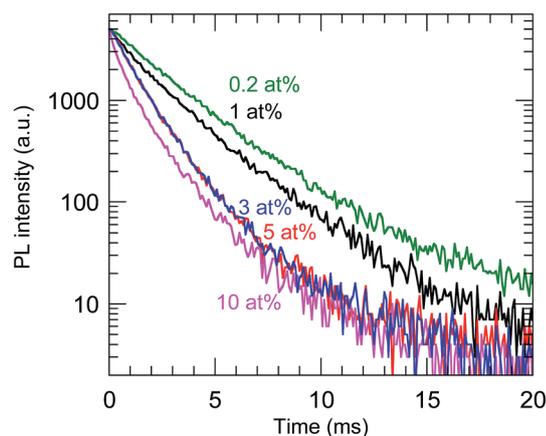**Fig. 9** PL decay curves of the calcined samples codoped with 0.2–10 at% Bi^{3+} and 2 at% Eu^{3+}. λ_{ex} = 365 nm and λ_{em} = 612 nm.

Table 2 PL lifetimes of the calcined samples codoped with 0.2–10 at% Bi^{3+} and 2 at% Eu^{3+} calculated from the decay curves

Nominal Bi (at%)	τ_1 (ms)	τ_2 (ms)	τ (ms)
0.2	2.28	5.07	2.80
1.0	1.24	2.77	2.29
3.0	1.07	2.41	1.37
5.0	1.06	2.27	1.37
10	0.49	1.64	1.19

where I is the PL intensity at time t, τ_1 and τ_2 are the short and long PL lifetimes, and A_1 and A_2 are constants. The two PL lifetime components imply two different Eu^{3+} luminescence centers. As mentioned above, the most likely luminescent centers for the emission at 612 nm are Eu^{3+} ions at the C_2 sites and the surface sites. Generally, the surface sites have shorter lifetimes than the lattice sites because of surface defects. Therefore, τ_1 can be assigned to the surface sites and τ_2 to the C_2 sites. The average lifetime τ was calculated by eqn (3):

4 Conclusions

We produced Y_2O_3:Bi^{3+},Eu^{3+} nanosheets through calcining solvothermally-synthesized LYH nanosheets. XRD and TEM analysis revealed that the LYH nanosheets were composed of

crystallites with a uniform crystallographic orientation. Their sheet-like morphology and single-crystal nature remained after calcination, while the thickness of the nanosheets decreased from 40 nm to 25 nm. The PL and PLE spectra of the Y_2O_3:Bi^{3+},Eu^{3+} nanosheets exhibited red emission from Eu^{3+} following energy transfer from photoexcited Bi^{3+} to Eu^{3+}. The PL QY of the Y_2O_3:Bi^{3+},Eu^{3+} nanosheets with fixed Eu^{3+} concentrations of 2 at% was dependent on the Bi content, with the highest QY being 23%, in the sample with a Bi concentration of 0.2 at%. The PL lifetimes of the calcined samples with Bi^{3+} concentrations of ≥0.2 at% decreased with increasing Bi concentration because of concentration quenching. However, for each sample, the PL intensity under continuous excitation increased over time. This may be attributable to the photooxidation of bismuth in low oxidation states following its reduction by PEI or methanol during the LYH synthesis.

Acknowledgements

References

1 J. Liu, X. Zou, B. Xu, H. Luo, H. Lv, L. Han and X. Yu, *CrystEngComm*, 2012, **14**, 3149–3155.

2 A. Towata, M. Sivakumar, K. Yasui, T. Tuziuti, T. Kozuka and Y. Iida, *J. Mater. Sci.*, 2008, **43**, 1214–1219.

3 B. Lu, J. Li, T. Suzuki, M. Estili, W. Liu, X. Sun and Y. Sakka, *J. Am. Ceram. Soc.*, 2015, **98**, 1413–1422.

4 L. S. Chi, R. S. Liu and B. J. Lee, *J. Electrochem. Soc.*, 2005, **152**, J93–J98.

5 W. J. Park, S. G. Yoon and D. H. Yoon, *J. Electroceram.*, 2006, **17**, 41–44.

6 G. Ju, Y. Hu, L. Chen, X. Wang, Z. Mu, H. Wu and F. Kang, *J. Electrochem. Soc.*, 2011, **158**, J294–J299.

7 T.-S. Chan, C.-C. Kang, R.-S. Liu, L. Chen, X.-N. Liu, J.-J. Ding, J. Bao and C. Gao, *J. Comb. Chem.*, 2007, **9**, 343–346.

8 K. Ohno, Phosphors for cathode-ray tubes, *Phosphor Handbook*, CRC Press LLC, Boca Raton, 1999, pp. 489–498.

9 C. Strumpel, C. McCann, G. Beaucarne, G. Arkhipov, A. Slaoui, V. Svrcek and C. Canizo, *Sol. Energy Mater. Sol. Cells*, 2007, **91**, 238–249.

10 P. Chung, H. Chung and P. Holloway, *J. Vac. Sci. Technol., A*, 2007, **25**, 61–66.

11 N. Chander, A. F. Khan, P. S. Chandrasekhar, E. Thouti, S. K. Swami, V. Dutta and V. K. Komarala, *Appl. Phys. Lett.*, 2014, **105**, 033904.

12 C. K. Huang, Y. C. Chen, W. B. Huang, T. M. Chen, K. W. Sun and W.-L. Chang, *Prog. Photovoltaics. Res. Appl.*, 2013, **21**, 1507–1513.

13 E. Klampaftis, D. Ross, K. R. McIntosh and B. S. Richards, *Sol. Energy Mater. Sol. Cells*, 2009, **93**, 1182–1194.

14 B. M. Ende, L. Aartsa and A. Meijerink, *Phys. Chem. Chem. Phys.*, 2009, **11**, 11081–11095.

15 Y. Iso, S. Takeshita and T. Isobe, *J. Electrochem. Soc.*, 2012, **159**, J72–J76.

16 S. Takeshita, H. Ogata, T. Isobe, T. Sawayama and S. Niikura, *J. Electrochem. Soc.*, 2010, **157**, J74–J80.

17 S. Takeshita, T. Watanabe, T. Isobe, T. Sawayama and S. Niikura, *Opt. Mater.*, 2011, **33**, 323–326.

18 H. Hara, S. Takeshita, T. Isobe, T. Sawayama and S. Niikura, *Mater. Sci. Eng., B*, 2013, **178**, 311–315.

19 Q. Zhu, J.-G. Li, C. Zhi, R. Ma, T. Sasaki, J. X. Xu, C. H. Liu, X. D. Li, X. D. Sun and Y. Sakka, *J. Mater. Chem.*, 2011, **21**, 6903–6908.

20 H. Zhu, Y. Ma, H. Yang, P. Zhu, J. Du, C. Ji and D. Hou, *J. Solid State Chem.*, 2010, **150**, 1208–1212.

21 A. P. Jadhav, C. W. Kim, H. G. Cha, A. U. Pawar, N. A. Jadhav, U. Pal and Y. S. Kang, *J. Phys. Chem. C*, 2009, **113**, 13600–13604.

22 Q. Zhu, J.-G. Li, R. Ma, T. Sasaki, X. Yang, X. Li, X. Sun and Y. Sakka, *J. Solid State Chem.*, 2012, **192**, 229–237.

23 Q. Zhu, J.-G. Li, C. Zhi, X. Li, X. Sun, Y. Sakka, D. Golberg and Y. Bando, *Chem. Mater.*, 2010, **22**, 4204–4213.

24 F. Geng, H. Xin, Y. Matsushita, R. Ma, M. Tanaka, F. Izumi, N. Iyi and T. Sasaki, *Chem.–Eur. J.*, 2008, **14**, 9255–9260.

25 X. Wu, J.-G. Li, Q. Zhu, W. Liu, J. Li, X. Li, X. Sun and Y. Sakka, *J. Mater. Chem. C*, 2015, **3**, 3428–3437.

26 L. Hu, R. Ma, T. C. Ozawa and T. Sasaki, *Inorg. Chem.*, 2010, **49**, 2960–2968.

27 L. Hu, R. Ma, T. C. Ozawa and T. Sasaki, *Angew. Chem., Int. Ed.*, 2009, **48**, 3846–3849.

28 Q. Zhu, J. G. Li, X. Li, X. Sun, Y. Qi, M. Zhu and Y. Sakka, *Sci. Technol. Adv. Mater.*, 2014, **15**, 14203.

29 T. Matsunaga, S. Takeshita and T. Isobe, *J. Lumin.*, 2015, **165**, 62–67.

30 S. S. Lee, B. I. Lee, S. J. Kim, S. H. Byeon and J. K. Kang, *Inorg. Chem.*, 2012, **51**, 10222–10232.

31 J. Liang, R. Ma and T. Sasaki, *Dalton Trans.*, 2014, **43**, 10355–10364.

32 A. D. Yapryntsev, A. E. Baranchikov, L. S. Skogareva, A. E. Goldt, I. P. Stolyarov, O. S. Ivanova, V. V. Kozik and V. K. Ivanov, *CrystEngComm*, 2015, **17**, 2667–2674.

33 R. Cao, M. Peng and J. Qiu, *Opt. Express*, 2012, **20**, A977–A983.